The International Journal of Advanced Manufacturing Technology (2024) 130:3065–3079
https://doi.org/10.1007/s00170-023-12850-8

ORIGINAL ARTICLE

Analytical prediction of shot peening residual stress distribution using inherent strain in aluminum–magnesium alloy plates under various peening conditions

Takahiro Ohta[1] · **Ninshu Ma**[2]

Received: 30 August 2023 / Accepted: 10 December 2023 / Published online: 27 December 2023

Abstract
The compressive residual stress distribution in shot peening can be simulated using the nonlinear elastic–plastic finite element method (FEM) or obtained using various measurement methods; however, a simple and efficient prediction is desirable for practical applications. The residual plastic strain component produced by shot peening, known as the inherent strain or Eigenstrain, has a simple distribution and can be used to predict the residual stress via linear elastic analysis. In this study, the residual stress distributions in aluminum–magnesium alloy plates due to various shot velocities and shot diameters were simulated using the nonlinear FEM; further, the residual stress distributions were verified using the X-ray diffraction method. The inherent strain was identified using these results as datasets, and the strain distribution was quantitatively expressed using a simple equation. Finally, an analytical method for shot peening residual stress prediction using inherent strain and plate bending theory was developed. The residual stress distributions predicted from the inherent strain determined for 5 -mm-thick plate were consistent with the experimentally measured and numerical simulated results for 2-, and 1 -mm-thick plates with different shot blasting machines and shot diameters.

Keywords Shot peening · Residual stress · Shot velocity · Inherent strain · Eigenstrain · Finite element method

1 Introduction

Shot peening is widely used to improve the fatigue strengths of aircraft and automotive parts. Shot peening parameters include the diameter, material, velocity of the shot, impact angle, and coverage. In pneumatic shot peening, shot velocity is controlled by air pressure, nozzle shape, and shot mass flow. The relationship between these parameters and the compressive residual stress distribution has been clarified in several studies. Schiffner [1], Tao and Gao [2], Gallitelli et al. [3], and Li et al. [4] used numerical simulation to investigate the relationship between the residual stress distribution and shot diameter and velocity. Wang et al. [5], Zinn and Scholtes [6], and Miao et al. [7] experimentally investigated the relationship between the residual stress distribution and shot diameter. They demonstrated that the depths of the maximum residual compressive stress and compressive stress increase with shot velocity and diameter.

Moreover, the effects of shot diameter and velocity on the residual stress distribution have been quantitatively demonstrated. Al-Hassani [8] and Al-Obaid [9] established a relationship between the depth of plastic strain, shot velocity, and diameter at single shot impact. Ogawa and Asano [10] proposed an equation describing the relationship between the maximum residual compressive stress, shot velocity, diameter, and density. Robertson [11] presented a simple equation for the residual stress distribution after shot peening. Tao and Gao [2] proposed a method for predicting the residual stress distribution by correlating the coefficients of the equation proposed by Robertson [11] with shot velocity and diameter using up to third-order linear regression. Ohta et al. [12] expressed the coefficients of Robertson's equation as a simple function of shot diameter and shot velocity and they demonstrated that the residual stress distribution could be predicted under an unknown shot peening condition.

✉ Takahiro Ohta
t.ohta.62@cc.it-hiroshima.ac.jp

[1] Department of Mechanical System Engineering, Faculty of Engineering, Hiroshima Institute of Technology, 2-1-1 Miyake Saeki-Ku, Hiroshima 731-5193, Japan

[2] Joining and Welding Research Institute, Osaka University, 11-1 Mihogaoka, Ibaragi, Osaka 567-0047, Japan

However, the prediction equation using Robertson's equation can only be applied to a single thickness. Gallitelli et al. [3] proposed complex equations for surface stress, maximum compressive stress, and depth as functions of shot velocity, diameter, and density. Li et al. [4] obtained the optimal parameters by employing the Box–Behnken design response surface method for the shot velocity, standoff distance, and coverage using the finite element method.

The residual plastic strain produced by shot peening, known as the inherent strain (or eigenstrain), has a simple distribution, does not change even if the specimens are cut after shot peening, and can be used to reproduce the residual stress using linear elastic analysis. Fujimoto et al. [13], Ueda and Ma [14], Nakacho et al. [15], and Korsunsky [16] reported the relation of inherent strain to residual weld stress. The inherent strain $\{g\}$ can be expressed as $\{g\} = \{\varepsilon\} - \{\varepsilon_e\}$, where $\{\varepsilon\}$ and $\{\varepsilon_e\}$ are the total and elastic strains, respectively. The relationship between the residual stress $\{\sigma\}$ and inherent strain can be expressed as, $\{\sigma\} = [D][H^*]\{g\}$, where $[D]$ is the elastic stress–strain matrix and $[H^*]$ is the elastic response (inherent strain –elastic strain) matrix [13–15]. The residual stress corresponds elastically and uniquely to the inherent strain, which can be used to determine the residual stress distribution using linear elastic calculations.

Niku-Lari [17] proposed the stress source method to calculate residual stress in shot peening. Terasaki et al. [18] proposed a method for measuring the inherent strain generated by shot peening and measured the inherent strain distribution in plates and cylindrical objects. Kitamura et al. [19] explained the difference in residual stress due to the shot shape using inherent strain. Korsunsky [20] proposed a method to calculate the residual stress distribution using the inherent strain for shot peening and demonstrated its effectiveness. Korsunsky [21] measured the residual elastic strain of a laser shock-peened titanium alloy plate using high-energy synchrotron radiation X-ray diffraction and proposed a method to estimate the most likely inherent strain profile. Achintha and Nowell [22] simulated the residual stress induced by laser shock peening by modeling the shock wave as a dynamic pressure load with an explicit finite element and incorporating the plastic strain distribution as an inherent strain distribution in a static finite element model. Coratella et al. [23] investigated the feasibility of applying the inherent strain method to predict residual stresses in laser shock peening for samples with curved geometries. To simulate the effect and evolution of the residual stress during low-cycle fatigue, Song et al. [24] employed a finite element model considering both the inherent strain induced by shot peening and the effect of hardening on subsequent deformation. Salvati and Korsunsky [25] presented a method using inherent strain to predict the residual stress field produced by laser shock peening and carburizing material surfaces in three-dimensional geometries. Faucheux et al. [26] performed simulations using inherent strain in peen forming and stress peen forming and showed that the panel shape changed from spherical to cylindrical with decreasing panel thickness. Hu et al. [27] developed an inherent strain-based modeling procedure to simulate the prestress effects on the bending deformation and residual stresses in laser peen forming. Ohta et al. [28–30] simulated the deformation during peen forming by inputting the plastic strain obtained via the dynamic explicit finite element method during shot impact as an inherent strain into the static implicit method. Miao et al. [31] evaluated the effects of various sources of anisotropy in uniformly peen-formed aluminum sheets by using inherent strain and observed that the bending loads induced by the initial residual stresses in the rolling direction of the plate, resulted in uniformly peen-formed sheets.

In addition, these reports indicate that the method of calculating residual stress using inherent strain is effective in surface treatments such as shot peening and laser shock peening; however, the variation in the inherent strain distribution with shot peening conditions, such as shot diameter, shot velocity, and specimen thickness, has not been quantitatively investigated.

Therefore, in this study, an equation for estimating the residual stress distribution in shot peening is developed by considering the shot velocity, diameter, and specimen thickness. An estimation method for the residual stress distribution is established by using the inherent strain distribution and assuming that the inherent strain distribution can be expressed as a function of only the shot velocity and diameter. Because the inherent strain distribution is not affected by the geometry of the specimen, the advantage of this method is that the estimated inherent strain distribution from small-size specimens can be used to predict the residual stress distribution for practically large-size components or cut geometries for various purposes that have not been tested or simulated. In this study, the effect of thickness on residual stress was predicted using this method. Based on the residual stress distribution simulated using the finite element method (FEM), an inverse analysis of the inherent strain distribution was performed. The obtained residual stress distributions were verified using experimental results.

2 Residual stress calculation using inherent strain distribution

Directly measuring the inherent strain distribution is usually difficult. Therefore, residual stress measurements or numerical simulation results can be used to determine the inherent strain distribution using inverse analysis. The inherent strain distribution can be determined with a small number of coefficients by expressing the inherent strain distribution as a function. Ueda

and Ma [14] and Nakacho et al. [15] proposed a functional representation of the inherent strain distribution, which was effective in calculating the residual welding stress distribution in a small region. Salvati and Korsunsky [25] calculated the residual stresses using a Gaussian distribution of the inherent strain distribution within the thickness of shot peening. Song et al. [24] described the inherent strain distribution within the thickness of shot peening as a combination of two Gaussian distributions.

The x, y, and z directions represent the thickness, longitudinal, and width directions, respectively. In shot peening, the strain generated by the impact of steel balls is axisymmetric, so the inherent strain components g_y and g_z in the y and z directions are the same, and the distribution remains the same throughout the material. Therefore, the inherent strain at a depth of x from the surface is indicated as $g_{(x)}$. The inherent strain g_z in the thickness direction and the inherent shear strain components (g_{xy}, g_{yz}, g_{zx}) were not considered in this study because their contribution to the residual stress distribution is small. The inherent strain distribution $g_{(x)}$ within the thickness is described by the Gaussian distribution, as shown in Eq. (1):

$$g_{(x)} = \frac{A}{\sqrt{2\pi}S} exp\left\{ \frac{\left(x - X_d\right)^2}{2S^2} \right\} \tag{1}$$

where x is the depth from the peened surface; A is a coefficient indicating the area of inherent strain distribution; S and X_d are coefficients indicating the depth and depth of peak of inherent strain distribution, respectively.

As shown in Fig. 1, the inherent z-directional stress $\sigma_z{}^*$ and y-directional stress $\sigma_y{}^*$ occur when external force F_0 and bending moment M_0 are applied to the material to prevent elongation and bending (in the fully constrained case). Because $\sigma_z{}^*$ and $\sigma_y{}^*$ are equal, the inherent stress at depth x is denoted as $\sigma_{1(x)}$ and is expressed as shown in Eq. (2):

$$\sigma_{1(x)} = -\frac{1+\nu}{1-\nu^2} E g_{(x)} \tag{2}$$

where E is Young's modulus, and ν is Poisson's ratio. Figure 2 shows the distribution of $\sigma_{1(x)}$ calculated using Eq. (2)

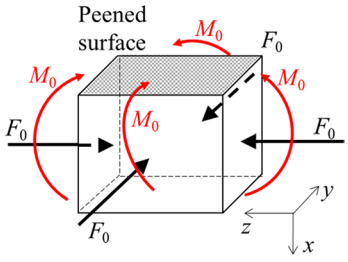

Fig. 1 Constraints for Eq. (2)

assuming the inherent strain distribution ($A = 0.001$ mm, $S = 0.15$ mm, $X_d = 0.10$ mm), $E = 70$ GPa, and $\nu = 0.3$. The compressive stresses correspond to the inherent strain.

The external force F_0 restrains elongation in the y- and z-directions. A force in the opposite direction of F_0 generates stress as calculated in Eq. (3). Stresses in the y- and z-directions are equal and are denoted by $\sigma_{2(x)}$ and can be calculated as per Eq. (3):

$$\sigma_{2(x)} = -\frac{\int_0^h \sigma_{1(x)} b dx}{hb} \tag{3}$$

where h is the thickness and b is the width. Figure 2 shows the distribution of $\sigma_{2(x)}$ calculated by applying Eq. (3). The tensile stress is constant within the thickness and is balanced by the force generated by $\sigma_{1(x)}$.

The bending moment M in the y- and z-directions is opposite to the bending constraint M_0, and the peened surface is deformed convexly. y- and z-direction bending moments are equal and are denoted as M. The bending moment in the x- and y-directions is denoted as M. M is calculated using Eq. (4) as follows:

$$M = \int_0^h \sigma_{1(x)} b(x - h/2) dx \tag{4}$$

The bending moment causes the deformation of the plate. M causes the plate to bend to the same radius of curvature R in the y- and z- directions, deforming it into a spherical shape. The radius of curvature R is given by Eq. (5), as follows:

$$R = \frac{Ebh^3(1+\nu)}{12M\left(1-\nu^2\right)} \tag{5}$$

M causes bending stresses $\sigma_{3(x)}$ in the y- and z-directions. $\sigma_{3(x)}$ is shown in Eq. (6):

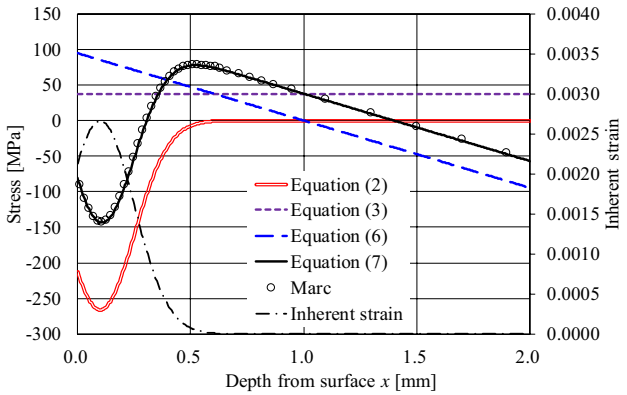

Fig. 2 Distribution of residual z-direction stress in the thickness calculated from the inherent strain distribution. Plots show the result simulated by FEM using Marc

$$\sigma_{3(x)} = \frac{E(1+\nu)}{1-\nu^2}\frac{(x-h/2)}{R} \tag{6}$$

Figure 2 shows the distribution of $\sigma_{3(x)}$ calculated using Eq. (6). The peened surface shows tensile stress, and the back surface shows compressive stress.

The residual stress distribution within the thickness is the sum of $\sigma_{1(x)}$, $\sigma_{2(x)}$, and $\sigma_{3(x)}$ as expressed in Eq. (7):

$$\sigma_{(x)} = \sigma_{1(x)} + \sigma_{2(x)} + \sigma_{3(x)} \tag{7}$$

The aforementioned equations can be used to analyze the residual stress distribution in the thickness based on the inherent strain distribution. Figure 2 shows the calculated residual stress distribution within the thickness based on the inherent strain distribution. In this example, the bending deformation is pronounced because $h = 2$ mm, and R, calculated using Eq. (5), is approximately 1058 mm. The residual stress distribution varies depending on the thickness even with the same inherent strain distribution.

Elasticity calculations were performed using the static implicit finite element method to validate these equations. Marc was the finite element method (FEM) code used. Figure 3 shows the finite element (FE) model of the validation of these calculations. The dimensions of the model were 76 mm (length) × 19 mm (width) × 2 mm (thickness). Three nodes were constrained to prevent rigid body movement. A composite element was used and divided into layers of a thickness of 0.02 mm up to 0.6 mm from the surface, and layers with thicknesses of 0.05 mm and 0.2 mm thereafter. The composite shell element allows the spacing of the integration points (layers) to be freely changed, and physical property values can be entered for each layer. The inherent strain was input for each layer as virtual thermal strain. The inherent strain distribution, E and ν, are the same as those shown in Fig. 2. The FEM results are shown in Fig. 2. The calculation and FEM results are consistent with the equations, and therefore, the proposed equations are validated. The use of inherent strain enables the simulation of the residual stress distribution via elasticity calculations.

This study shows that the residual stress distributions can be analyzed for various peening conditions and thicknesses by expressing A, S, and X_d as functions of shot diameter and shot velocity.

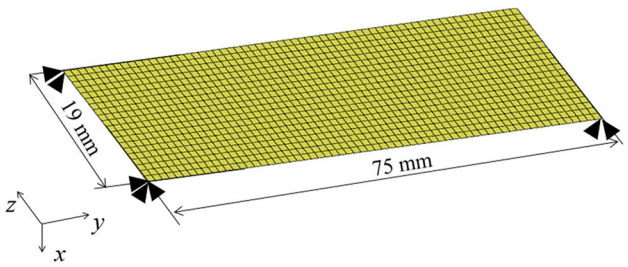

Fig. 3 FE model for validation of equations using Marc

3 Finite element model

Numerical simulations were performed using the FEM to determine the inherent strain distribution. The FEM was simulated in two steps using LS-DYNA [32, 33]. In the first step, a dynamic explicit method was used to simulate shot collisions. Owing to the oscillation of the stresses in the dynamic explicit method, equilibrium stresses were simulated in the second step using the static implicit method. The conditions used for the numerical simulations are listed in Table 1. Figure 4 shows the FE model. Three different shot diameters were used. Further, h was 5 mm, and the model dimension L was nine times the shot diameter. The dimension l of the region where the shot was impacted was three times the shot diameter. The number of elements was maintained constant. The element size near the surface of the shot impact area was 0.0195 mm in the depth direction and 0.0938 times the shot diameter in the length and

Table 1 Shot peening conditions for the FEM

Shot diameter [mm]	Shot velocity [m/s]	Number of shots
0.3	10, 19, 26, 35, 46, 65, 75	200
0.5	10, 15, 22, 30, 35, 44, 70	200
0.7	10, 15,20, 35, 44	200

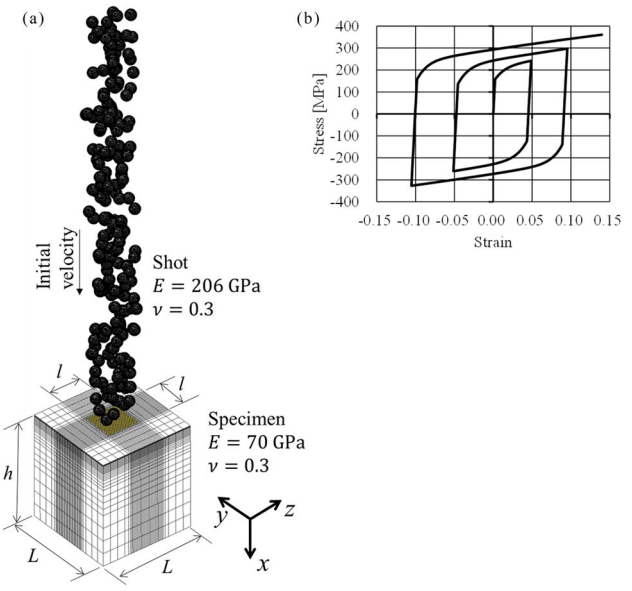

Fig. 4 FE model (**a**) FE model and (**b**) Stress–strain curve of the specimen

width directions. In the first step, the bottom surface was constrained in the *x*-direction, except in the region where the shots were impacted to prevent the oscillation of the FE model. In the second step, only three nodes were constrained to prevent rigid body movement, leaving the bottom surface free.

To reduce simulation time, the shots were placed such that they overlapped with each other, as shown in Fig. 4. The shots were given with an initial velocity. The shots were randomly positioned and spaced 0.2 times the shot diameter in the height direction to prevent two shots from colliding simultaneously. The shot was elastic, and was made of steel. Further, $E = 206$ GPa, $\nu = 0.3$, and density $\rho = 7.0 \times 10^{-9}\text{ton/mm}^3$. The Coulomb coefficient of friction between the shot and the specimen was set to 0.2.

The specimen material was an aluminum–magnesium alloy (A5052-H34) with $E = 70$ GPa, $\nu = 0.3$, and $\rho = 2.7 \times 10^{-9}\text{ton/mm}^3$. The stress–strain curve of the material is shown in Fig. 4b. The mixed hardening law was used because repetitive loading was applied during shot peening.

4 Experimental method

One direct-pressure-type and two suction-type shot blasting machines were used in the experiment. The shots were made of low-alloy steel that included manganese and silicon with a hardness of 45–52 HRC. The specimen was an aluminum-magnesium alloy (A5052-H34) plate, and its dimensions were as follows: width = 19 mm, length = 70 mm, and thickness = 5 or 2 mm. This alloy had a hardness of 68–70 HV, proof stress of 188 MPa, and tensile strength of 244 MPa. A5052-H34 was formed by the solid solution strengthening of magnesium and work hardening by cold working and did not undergo transformation owing to temperature increase or plastic deformation. Using steel shots on aluminum alloys may result in poor corrosion resistance. For example, Zupanc and Grum [34] shot peened aluminum alloy A7075-T651 using steel shot to investigate the effect of pitting corrosion on fatigue strength and reported that shot peening improved fatigue strength. Aghaie-Khafri et al. [35] shot-peened aircraft aluminum alloy parts (aircraft wheels) using steel shots and confirmed an increase in service life. Because steel shot has been used in aluminum alloys, this study used low-alloy steel shots (Aerospace Material Specifications 2431/1D: ASR70, ASR170, and ASR230) to determine the effects of shot diameter and shot velocity on the residual stress distribution.

The experimental conditions are listed in Table 2. The shot velocity was calculated by recording the flight of the shot using a high-speed camera and particle image velocimetry [12, 32, 33]. In Table 2, shot velocities are listed with the standard deviation of the measurement. In the direct-pressure-type machine, ASR170 and ASR230 had different shot mass flow; therefore, ASR230, which had a larger shot diameter, had a higher shot velocity. The nozzle hole diameters of the suction type-A and -B were different, and type-B had a higher shot velocity. The coverage was set to 200% for each condition.

The residual stress was measured by the X-ray diffraction method using device μ-X360 (Pulstec Co., Ltd.) based on the cosα scheme [36]. The diffraction peak of the (311) plane of aluminum in the Cr Kα line was used. The incident angle of the X-ray beam was 25°and the diffraction angle was 139.497°. Young's modulus and Poisson's ratio of the specimens were set to 69.31 GPa and 0.348, respectively; the values were entered as standard in the μ-X360. The X-ray beam diameter used in the residual stress measurement was approximately 2 mm. Electropolishing and stress measurements were repeatedly performed to measure the residual stress distribution inside the plate. Stress changes caused by electropolishing were corrected using the method suggested by Moore and Evans [37]. The maximum standard deviation of the measured residual stress was 15 MPa. One specimen was used for each shot peening condition, and residual stresses were measured in *z*- and *y*-directions at the same depth. Because significant difference in stresses was not observed between the *z*- and *y*-directions, the stresses

Table 2 (Continued)

Shot blasting machine	Shot	Mean shot diameter *D* [mm]	Air pressure [MPa]	Shot velocity *V* [m/s]	Thickness *h* [mm]
Direct-pressure-type	ASR170	0.5	0.14	30.2 ± 4.0	5
			0.30	43.8 ± 4.9	
	ASR230	0.7	0.14	36.9 ± 4.4	5
					2

Table 2 Experimental conditions

Shot blasting machine	Shot	Mean shot diameter *D* [mm]	Air pressure [MPa]	Shot velocity *V* [m/s]	Thickness *h* [mm]
Suction-type A	ASR70	0.3	0.2	9.5 ± 4.5	5
			0.6	25.5 ± 7.3	
	ASR170	0.5	0.2	8.3 ± 4.6	5
			0.6	22.4 ± 6.9	
	ASR230	0.7	0.2	7.6 ± 3.8	5
			0.6	20.5 ± 5.6	
Suction-type B	ASR70	0.3	0.2	30.7 ± 7.8	2
			0.5	63.2 ± 11.5	

in the z- and y-directions were indistinguishably treated in this study.

5 Finite element method results and inverse analysis of inherent strain distribution

5.1 Inverse analysis of inherent strain distribution

Figure 5 shows the residual stress contours simulated using the FEM for shot diameter $D=0.5$ mm, shot velocity $V=30$ m/s, a number of shots $N=200$, and thickness $h=5$ mm. Only the area ($l \times l$) impacted by shots is shown. On the peened surface, low tensile and high compressive stresses were mixed over a small area. The same results were obtained from the FEM by Ohta et al. [32, 33] and residual stress measurements performed in a small area by Yasukawa et al. [38]. Compressive stresses existed over the entire surface inside the material near the surface. The stress distributions in the z- and y-directions were different, though they were equivalent on average. Therefore, the z-direction stress was used in this study.

Figure 6 shows the FEM results of the residual stress distribution. The FEM results were used to plot the stress for all elements. The stresses in each element near the peening surface were distributed from tensile to compressive. The coefficients A, S, and X_d of the Gaussian distribution in Eq. (1), which minimizes the sum of the squares of the errors between the stresses in each element and the stress analyzed using Eq. (7), were determined. The stress analyzed using Eq. (7) is represented by the line.

The FEM simulated residual stresses exhibited a large range near the surface, even at the same depth. Regression analysis was performed to examine the plausible distributions. Residual stress distributions were examined by regression analysis using machine learning. Gaussian kernel support vector regression (SVR) was used to perform the regression analysis. The Gaussian kernel SVR requires the specification of hyperparameters (relaxation factor C, margin ε, and inverse of variance γ) to determine the learning range, which can be arbitrarily specified. C is a coefficient that determines how much error is tolerated in classification during training. ε is the margin, which indicates the error insensitivity zone. The inverse of the variance, γ, is used to adjust the accuracy of the training data. The SVR was performed using Python's Scikit-Learn library [39].

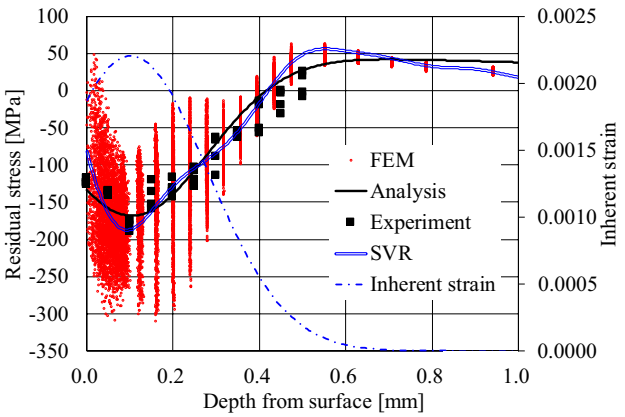

Fig. 6 Distribution of residual z-direction stress simulated using FEM and inversely analyzed inherent strain as well as reproduced z-direction stress when $D=0.5$ mm and $V=30$ m/s. Marks show experimentally measured z- and y-direction stress using ASR170 at $V=30.2\pm4.0$ m/s

Figure 6 displays the results of the SVR with a double line. A total of 29,696 depth and residual stresses in the FE model were used as training data for supervised learning. The hyperparameters were determined using a grid search to minimize the sum of squares of the errors. The following values were used: $C=500$, $\varepsilon=3$, and $\gamma=30$. The SVR results of the FEM data and the residual stress distribution analyzed using Eq. (7) were consistent.

The plot shows the residual stress distribution measured when ASR170 was projected at 0.2 MPa, in the direct-pressure type machine. The measured results of the residual stress distribution were consistent with the FEM results and the analysis results obtained using Eq. (7).

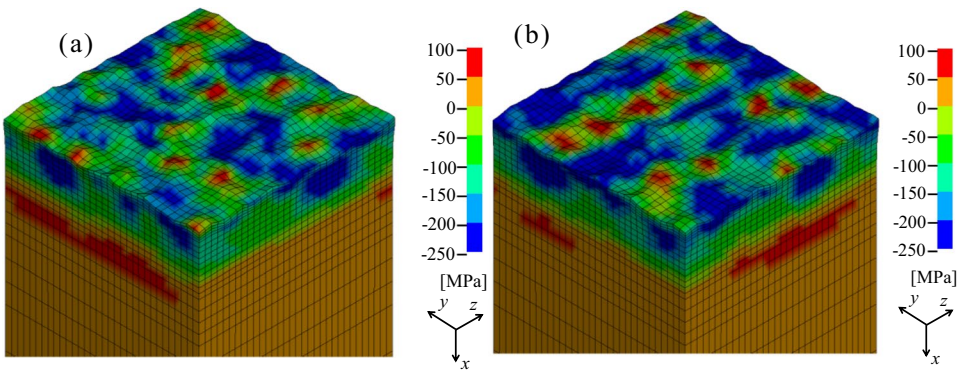

Fig. 5 Residual stress contours simulated using FEM when shot diameter $D=0.5$ mm and shot velocity $V=30$ m/s (**a**) z-direction stress, and (**b**) y-direction stress

As described earlier, if A, S, and X_d are determined such that the sum of squares of the errors between the residual stress distributions analyzed using the FEM and Eq. (7) are minimized, an inverse analysis of the inherent strain distribution can be performed.

5.2 Results of residual stress distribution

Inverse analysis was performed to obtain the inherent strain distribution from the FEM residual stress distribution, as shown in Fig. 6. Figure 7a shows the inherent strain distribution when $h=5$ mm and $D=0.3$ mm. As the shot velocity increases, the peak of inherent strain is located at a greater depth and is larger. The depth at which inherent strain is introduced also increases. In Fig. 7b, the lines show the analyzed residual stress distribution, and the plots show the experimental results using ASR70. Corresponding to the inherent strain, the location of the peak of the compressive residual stress is more deeply located and the peak is larger as the shot velocity increases. The depth at which compressive residual stress is introduced also increases. The experimental and analyzed residual stress distributions are in good agreement.

Figures 8a and 9a show the inherent strain distributions at $D=0.5$ mm and $D=0.7$ mm, respectively. The relationship between the shot velocity and inherent strain distribution is the same for $D=0.3$ mm. As the shot diameter increases, the peak position of the inherent strain becomes deeper, and the peak value increases. The depth at which the inherent strain is introduced also increases with an increasing shot diameter. At $D=0.7$ mm and $V=44$ m/s, the depth at which inherent strain is introduced is approximately 1.2 mm. Figures 8b and 9b show the residual stress distributions at $D=0.5$ and 0.7 mm, respectively. The lines show the analyzed residual stress distribution, and the plots show experimental results using ASR170 in Fig. 8b and ASR230 in Fig. 9b. Corresponding to the inherent strain, the peak of the compressive residual stress is located at a greater depth and becomes larger as the shot diameter increases. The depth at which compressive residual stress is introduced also increases. The

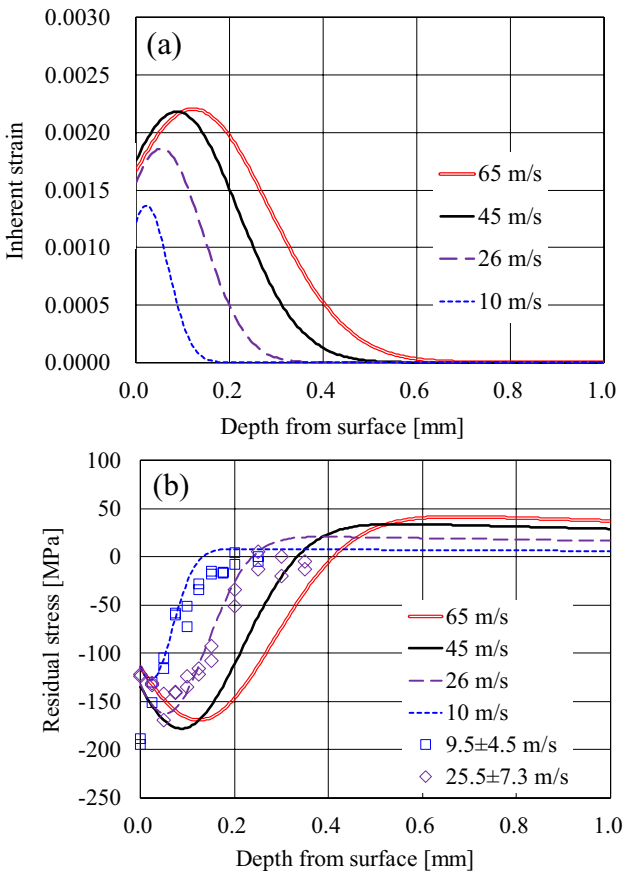

Fig. 7 Effect of shot velocity on inherent strain and residual z-direction stress distribution calculated by reverse analysis when $D=0.3$ mm and $h=5$ mm. Marks show experimentally measured z- and y-direction stress using ASR70. **a** Inherent strain distribution, and **b** residual stress distribution

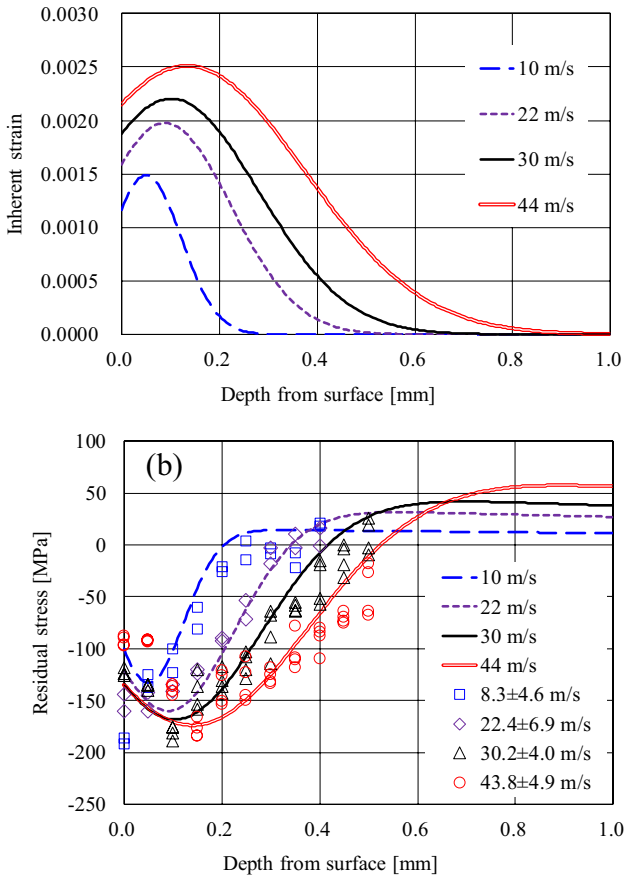

Fig. 8 Effect of shot velocity on inherent strain and residual z-direction stress distribution calculated using reverse analysis when $D=0.5$ mm and $h=5$ mm. Marks show experimentally measured z- and y-direction stress using ASR170. **a** Inherent strain distribution, and **b** residual stress distribution

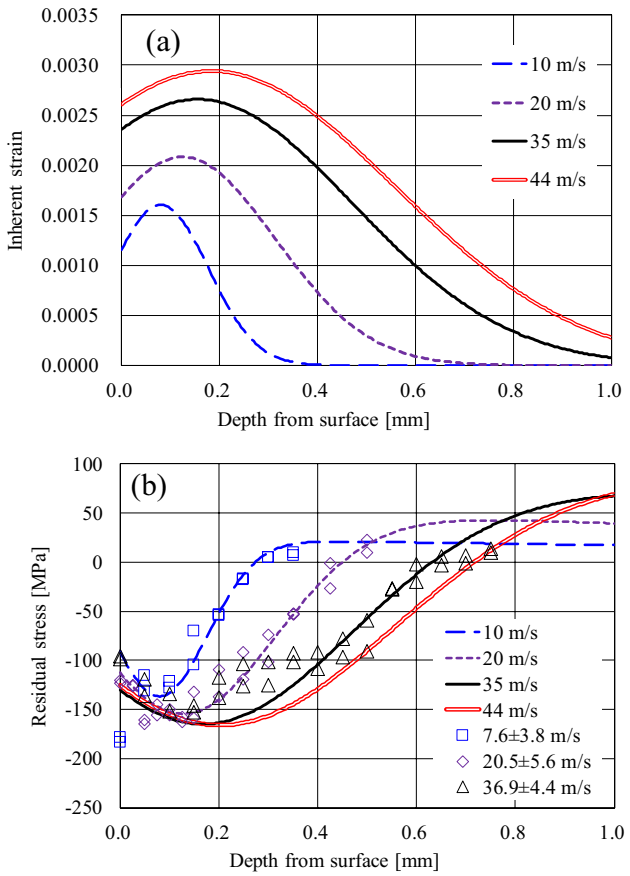

Fig. 9 Effect of shot velocity on inherent strain and residual z-direction stress distribution calculated using reverse analysis when $D=0.7$ mm and $h=5$ mm. Marks show experimentally measured z- and y-direction stress using ASR230. Inherent strain distribution, and **b** residual stress distribution

experimental and analyzed residual stress distributions are in good agreement, although shot peening is performed using different experimental machines.

5.3 Relationship between inherent strain distribution, shot diameter, and shot velocity

The inherent strain distribution is described by the Gaussian distribution shown in Eq. (1). The relationships between coefficients A, S, and X_d, shot diameter D, and shot velocity V were investigated. After attempting several approximation equations, the method of approximating shot velocity by a quadratic equation and shot diameter by a power function was selected in this study because it yields small error and the few coefficients. To identify the three coefficients of the quadratic equation, three levels of shot velocity in experiments are sufficient. More than three levels of experiments can be better to evaluate the function-fitting error. Figure 10 illustrates the relationship between A, D, and V. A is a coefficient indicating the area ($\int g_{(x)}dx$), which increases with V and D. The relationship between A and V was approximated using a quadratic equation, and the relationship between A and D was approximated using an n-power equation, as indicated by the lines in Fig. 10. The approximate equation is shown in Eq. (8), as follows:

$$A_{(D,V)} = \left(-5.316\times10^{-4}V^2 + 1.495\times10^{-1}V - 8.286\times10^{-1}\right)D^{1.647} \quad (8)$$

The unit for V is m/s, D is mm, and A is μm.

Figure 11 shows the relationship between S, D, and V; S is a coefficient that indicates the spread of the inherent strain distribution. S increases with increasing D and V. Similar to A, the lines approximated by Eq. (9) are shown in Fig. 11.

$$S_{(D,V)} = \left(-7.367\times10^{-5}V^2 + 1.617\times10^{-2}V + 1.791\times10^{-3}\right)D^{1.229} \quad (9)$$

The unit for V is m/s, D is mm, and S is mm.

Figure 12 shows the relationship between X_d, D, and V. X_d, is a coefficient indicating the depth of the inherent strain

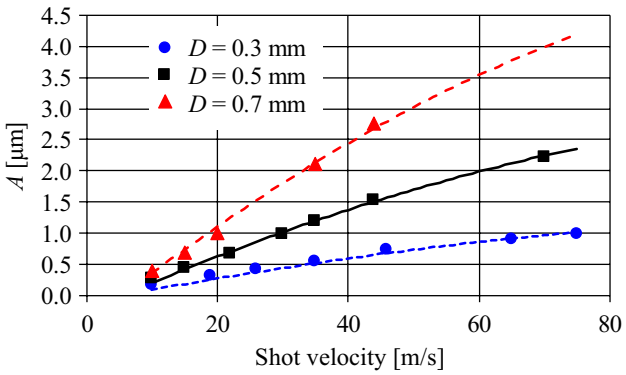

Fig. 10 Relationship between coefficient A in Eq. (1) obtained by inverse analysis from FEM results, and shot diameter D and shot velocity V

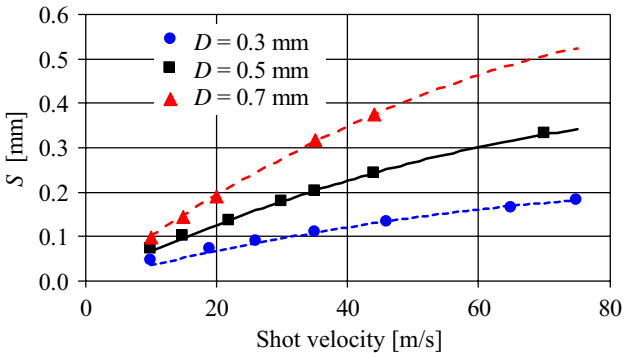

Fig. 11 Relationship between coefficient S in Eq. (1) obtained by inverse analysis from FEM results, and shot diameter D and shot velocity V

peak. X_d, increases with increasing D and V. Similar to A, the lines approximated by Eq. (10) are shown in Fig. 12.

$$X_{d(D,V)} = \left(3.270 \times 10^{-6} V^2 + 4.023 \times 10^{-3} V + 7.229 \times 10^{-2}\right) D^{0.921} \quad (10)$$

The unit for V is m/s, D is mm, and X_d is mm.

As described previously, the relationship between the coefficients shown in Eq. (1), D, and V can be expressed using an approximate formula. Even under conditions that have not been simulated via the FEM, the inherent strain distribution can be analyzed using Eqs. (8)–(10). However, the applicability is limited to the range of conditions for which the FEM simulations are conducted.

6 Verification of the prediction of the residual stress distribution

In the previous chapter, the effects of shot velocity and diameter on the inherent strain distribution were formulated for a 5 mm-thick specimen. This chapter presents that the inherent strain distribution determined for a 5 -mm-thick specimen is valid for different thicknesses assuming that the inherent strain distribution is not affected by thickness. Therefore, we verified the results of the residual stress distribution analysis by varying the thickness under three peening conditions.

6.1 Verification at $D = 0.3$ mm and $V = 30$ m/s.

FEM simulations were performed by varying the thickness under conditions not included in Table 1. The FE model is the same as that shown in Fig. 4 except for the thickness. The element sizes near the peened surface are the same. When $D = 0.3$ mm, and $V = 30$ m/s, the FEM results for thickness $h = 2$ and 1 mm are shown in Figs. 13 and 14, respectively. Under these conditions, the depth of the inherent strain $(3S + X_d)$ is approximately 0.3 mm. The FEM results are used to plot the stress for all elements. The residual stress distribution analyzed from the inherent strain distribution determined at $h = 5$ mm using Eqs. (8), (9), and (10) is represented by the line in the figure. The residual stress distribution analyzed from the approximated inherent strain distribution is in close agreement with the FEM results. Figure 13 shows the experimental results at $V = 30.7 \pm 7.8$ m/s using ASR70. The experimental and analyzed results are in good agreement.

The shot-blasting machines used, as shown in Figs. 7 and 13, are different; however, the same inherent strain distribution equation can be applied using the shot velocity.

The inherent strain distribution is predicted from the FE model with $h = 5$ mm. However, under these peening conditions, the same inherent strain distribution can be applied up to $h = 1$ mm. Therefore, it can be inferred that the inherent strain distribution is not affected by the thickness.

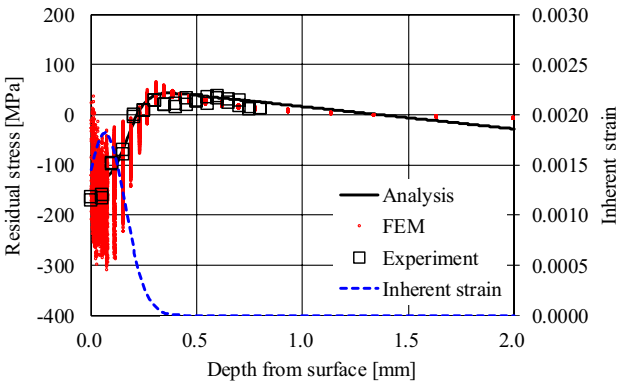

Fig. 13 Residual z-direction stress distribution simulated using FEM and analyzed by inherent strain distribution approximated at $h = 5$ mm using Eqs. (8)–(10) when $D = 0.3$ mm, $h = 2$ mm, and V is 30 m/s. Marks show experimentally measured z- and y-direction stress using ASR70 at $V = 30.7 \pm 7.8$ m/s

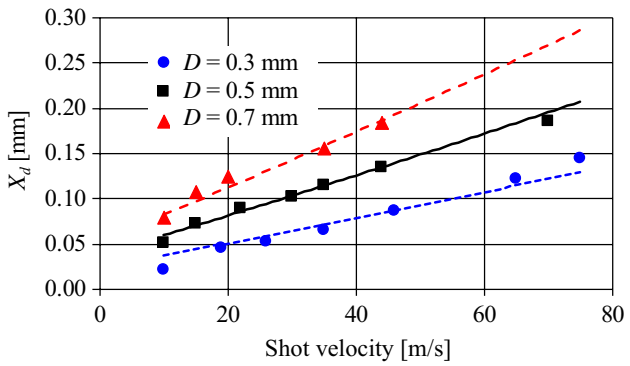

Fig. 12 Relationship between coefficient X_d in Eq. (1) obtained by inverse analysis from FEM results, and shot diameter D and shot velocity V

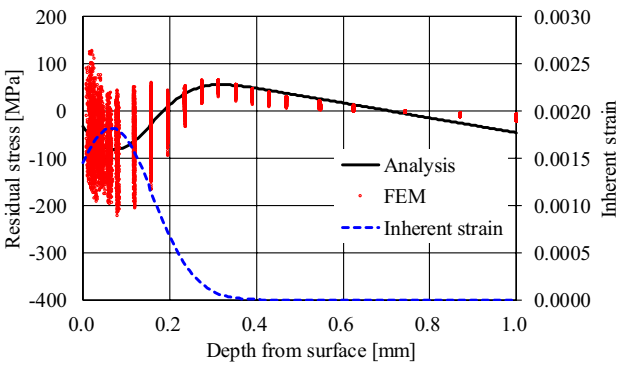

Fig. 14 Residual z-direction stress distribution simulated using FEM and analyzed by inherent strain distribution approximated at $h = 5$ mm using Eqs. (8)–(10) when $D = 0.3$ mm, $h = 1$ mm, and $V = 30$ m/s

6.2 Verification at $D=0.3$ mm and $V=65$ m/s.

The study was conducted at $D=0.3$ mm and $V=65$ m/s, which is the maximum shot velocity. The FEM results for thicknesses $h=2$ and 1 mm are shown in Figs. 15 and 16, respectively. The FEM results are used to plot the stress for all elements. The residual stress distribution analyzed from the inherent strain distribution determined at $h=5$ mm using Eqs. (8), (9), and (10) is represented by the lines in the figure. Under this condition, the depth of the inherent strain ($3S+X_d$) is approximately 0.6 mm. Figure 15 shows the experimental results at $V=63.2\pm11.5$ m/s using ASR70. The residual stress distribution analyzed from the inherent strain distribution determined using Eqs. (8), (9), and (10) are consistent with the experimental and FEM results.

Under these peening conditions, the same inherent strain distribution can be applied up to $h=1$ mm. Therefore, it can be inferred that the inherent strain distribution is not affected by the thickness.

6.3 Verification at $D=0.7$ mm and $V=35$ m/s.

The analysis of the residual stress distribution in the region with a large shot diameter and high shot velocity is validated. At $D=0.7$ mm and $V=35$ m/s, the FEM results for thicknesses $h=5$, 2, and 1 mm are shown in Figs. 17, 18, and 19 respectively. The residual stress distribution analyzed from the inherent strain distribution determined at $h=5$ mm using Eqs. (8), (9), and (10) is represented by the lines in the figure. Under these conditions, the depth of inherent strain ($3S+X_d$) is approximately 1.1 mm. The experimental results obtained using ASR230 at $V=36.9\pm4.4$ m/s are plotted in Figs. 17 and 18. The residual stress distributions analyzed from the inherent strain distributions are consistent with the experimental and FEM results.

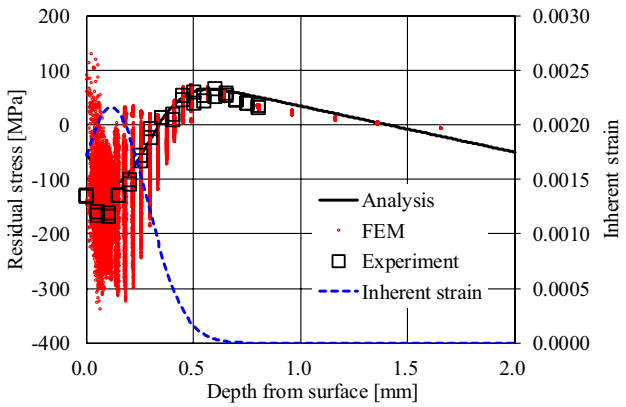

Fig. 15 Residual z-direction stress distribution simulated by FEM and analyzed by inherent strain distribution approximated at $h=5$ mm using Eqs. (8)–(10) when $D=0.3$ mm, $h=2$ mm, and $V=65$ m/s. Marks show experimentally measured z- and y-direction stress using ASR70 at $V=63.2\pm11.5$ m/s

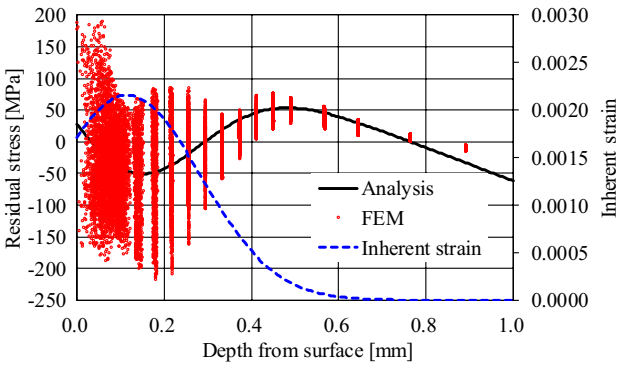

Fig. 16 Residual z-direction stress distribution simulated using FEM and analyzed by inherent strain distribution approximated at $h=5$ mm using Eqs. (8)–(10) when $D=0.3$ mm, $h=1$ mm, and $V=65$ m/s

Based on the above results, the approximations of the inherent strain distributions in Eqs. (8), (9), and (10) obtained from the simulations of the FE model with $h=5$ mm are valid for $h\geq1$ mm. The use of inherent strain distributions yields quantitative predictions of the effects of shot velocity and diameter on residual stress distributions at different thicknesses for which no experimental or numerical simulations were performed. This result is an advantage of this method.

7 Results calculated for steel plates

The method of calculating residual stresses using inherent strain was applied to Guagliano's results [40] for steel plate. These results were calculated using FEM with shot diameters of 0.3, 0.5, 0.7, and 1.0 mm and shot velocities of 40, 60,

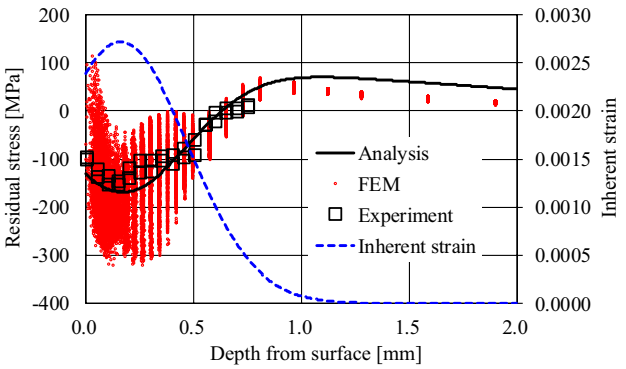

Fig. 17 Residual z-direction stress distribution simulated using FEM and analyzed by inherent strain distribution approximated at $h=5$ mm using Eqs. (8)–(10) when $D=0.7$ mm, $h=5$ mm, and $V=35$ m/s. Marks show experimentally measured z- and y-direction stress using ASR230 at $V=36.9\pm4.4$ m/s

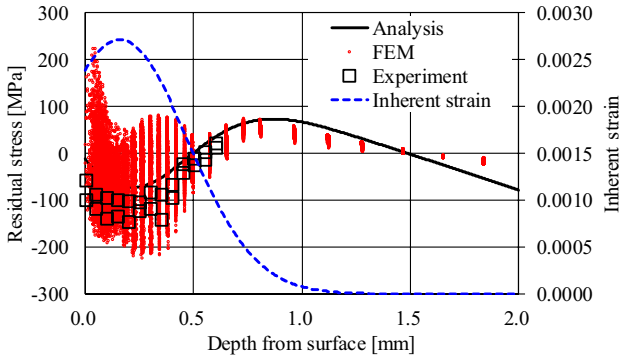

Fig.18 Residual z-direction stress distribution simulated using FEM and analyzed by inherent strain distribution approximated at $h=5$ mm using Eqs. (8)–(10) when $D=0.7$ mm, $h=2$ mm, and $V=35$ m/s. Marks show experimentally measured z- and y-direction stress using ASR230 at $V=36.9\pm4.4$ m/s

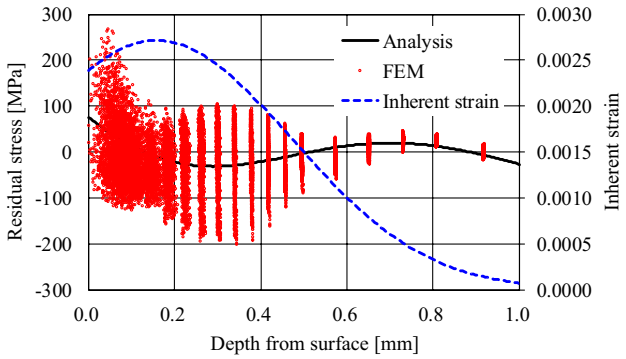

Fig.19 Residual z-direction stress distribution simulated using FEM and analyzed by inherent strain distribution approximated at $h=5$ mm using Eqs. (8)–(10) when $D=0.7$ mm, $h=1$ mm, and $V=35$ m/s

80, and 100 m/s for a 50-mm-thick 39NiCrMo3 steel plate (tensile strength: 1053 MPa, yield stress: 950 MPa). Young's modulus was set to 206 GPa and Poisson's ratio to 0.3. The inverse analysis for inherent strain was performed using the residual stress distributions obtained as the FEM results. The relationship between the coefficients, and shot velocity and shot diameter is expressed in Eqs. (11), (12), and (13).

$$A_{(D,V)} = \left(-4.416\times10^{-5}V^2 + 1.059\times10^{-2}V + 2.074\times10^{-4}\right)D^{0.7205} \quad (11)$$

$$X_{d(D,V)} = \left(1.006\times10^{-6}V^2 + 2.045\times10^{-4}V + 5.837\times10^{-2}\right)D^{0.7489} \quad (12)$$

$$S_{(D,V)} = \left(3.739\times10^{-6}V^2 + 2.016\times10^{-4}V + 5.568\times10^{-2}\right)D^{0.7604} \quad (13)$$

The unit for V is m/s, D is mm, A is μm, X_d is mm, and S is mm.

Figures 20 and 21 show the FEM results from Guagliano [40] and the inherent strain and residual stress distributions calculated using Eqs. (11), (12), and (13) for the shot diameter of 0.3 mm and 1.0 mm, respectively. Because the plate was 50 mm thick, little bending deformation occurred, and the calculated residual stresses showed compressive stresses near the surface and approximately zero residual stresses on the inside of the plate. The compressive stress distribution near the surface agrees well with the FEM and calculation results using the inherent strain for both $D=0.3$ and 1.0 mm.

FEM showed localized tensile stress just inside the depth where the compressive stress was zero, but no tensile stress was observed in the calculation from the inherent strain. Therefore, a new function of the distribution of inherent strain was introduced to better simulate the residual stress distribution. The function of the distribution of inherent strain is shown in Eq. (14).

$$g_{(x)} = \alpha\{\cos(\beta+\omega x)\}e^{-\gamma x} \quad (14)$$

α, β, ω, and γ are coefficients, which are determined to fit the FEM results.

Figure 22 shows the distribution of inherent strain and residual stress calculated using Eq. (14) when $D=1$ mm. The inherent strain distribution is tensile near the surface, with a small compressive strain below the depth at

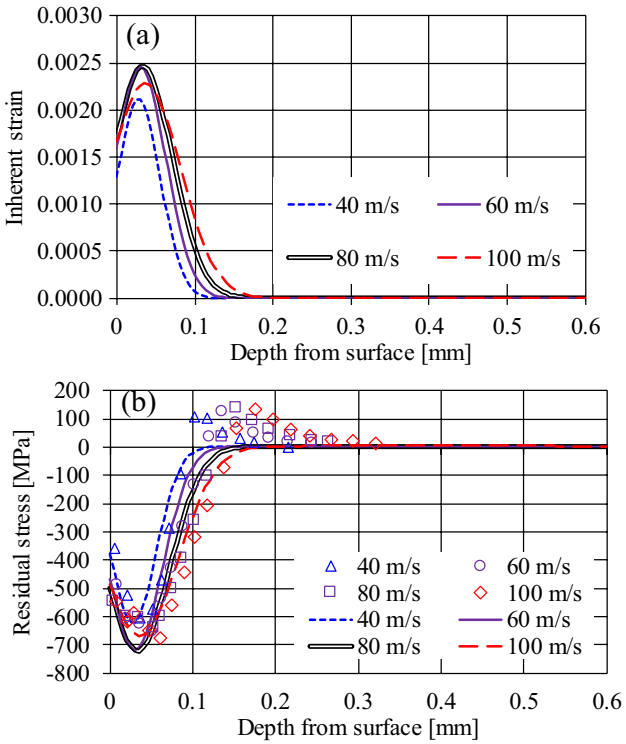

Fig. 20 Effect of shot velocity on inherent strain and residual z-direction stress distribution calculated by inverse analysis when $D=0.3$ mm and $h=50$ mm for 39NiCrMo3 steel plate. Marks show FEM results of Guagliano [40]. **a** Inherent strain distribution, and **b** residual stress distribution

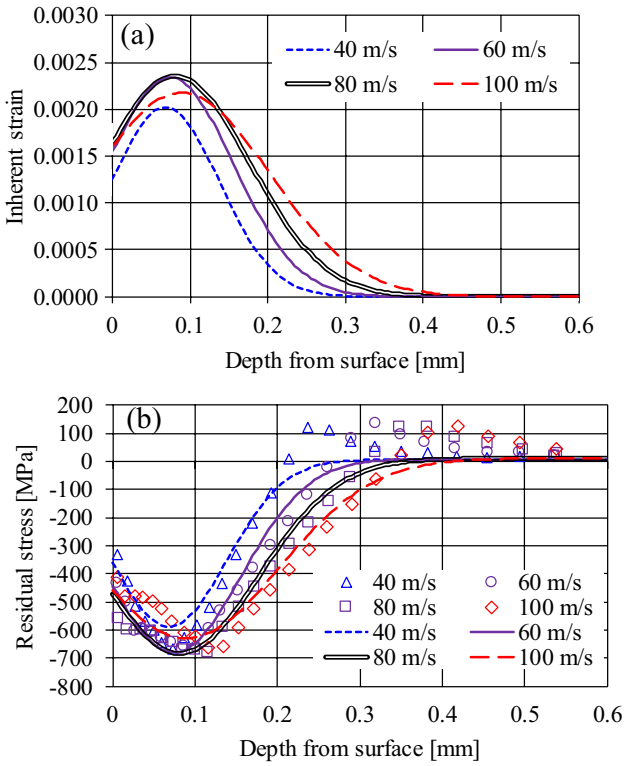

Fig. 21 Effect of shot velocity on inherent strain and residual z-direction stress distribution calculated by inverse analysis when $D=1.0$ mm and $h=50$ mm for 39NiCrMo3 steel plate. Marks show FEM results of Guagliano [40]. **a** Inherent strain distribution, and **b** residual stress distribution

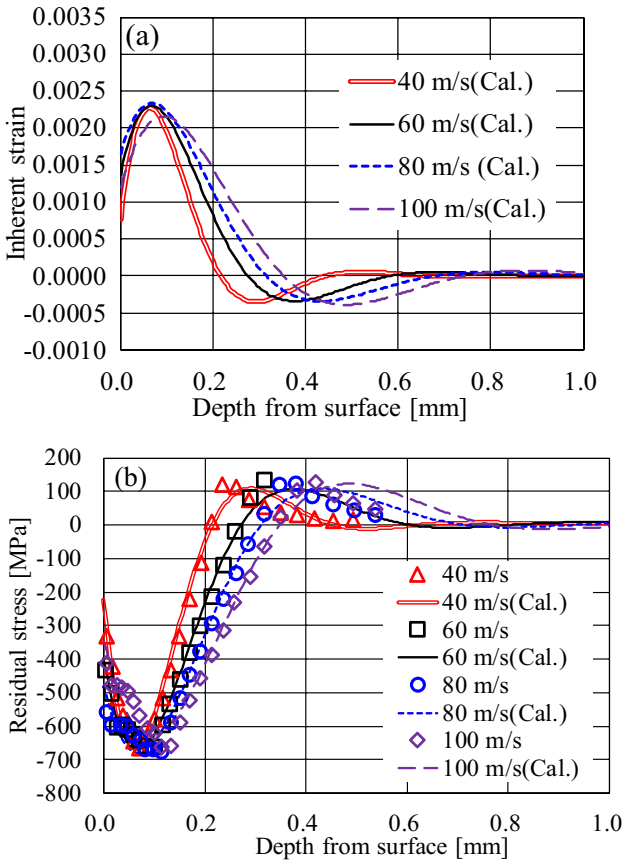

Fig. 22 Effect of shot velocity on inherent strain and residual z-direction stress distribution calculated by inverse analysis using Eq. (14) when $D=1.0$ mm and $h=50$ mm for 39NiCrMo3 steel plate. Marks show FEM results of Guagliano [40]. **a** Inherent strain distribution using Eq. (14), and **b** residual stress distribution

which tensile strain is zero. The difference between the FEM and calculated residual stress results is even smaller. For thicker plates, the inherent strain distribution using Eq. (14) agrees better with the FEM results than using Eq. (1).

Guagliano obtained the residual stress distribution in the Almen strip (type A, SAE 1070 steel, tensile strength: 1270 MPa, yield stress: 1120 MPa) using FEM and experiments [40]. The thickness of the Almen strip was 1.27 mm. Young's modulus was set to 206 GPa and Poisson's ratio to 0.3. The residual stress distribution for $D=0.3$ mm and $V=100$ m/s is shown in Fig. 23. The residual stress distribution, calculated from the inherent strain obtained by inverse analysis from FEM result using Eq. (1), is shown in Fig. 23a. The calculated results are in close agreement with the FEM results of Guagliano [40]. The radius of curvature calculated by Eq. (7) was 990 mm. When converted to arc height measured with an Almen gauge [41], it was 0.16 mm, which was smaller than the experimental result of 0.30 mm.

The residual stress distribution calculated from the inherent strain obtained by performing inverse analysis from experimental result using Eq. (1) is shown in Fig. 23b. The calculated results are in close agreement with the experimental results of Guagliano [40]. The radius of curvature calculated by Eq. (7) was 571 mm. The arc height measured with an Almen gauge was 0.28 mm, which was approximately equal to the experimental result of 0.30 mm. Inverse analysis is possible both from experimental results and FEM results.

As described earlier, a comparison with literature data [40] indicates that our method can be used for both aluminum alloy and steel.

8 Discussion

As shown in Chapter 6, the residual stress distributions for thicknesses of 1 mm and 2 mm can be calculated using the inherent strain distributions determined from the FEM results for a thickness of 5 mm.

Figure 24 demonstrates the effect of thickness on the residual stress distribution analyzed using inherent strain

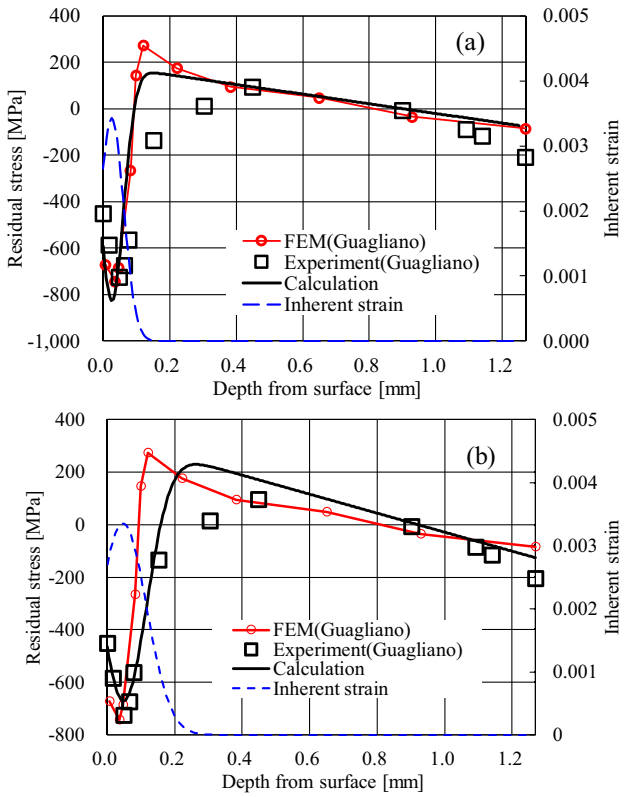

Fig. 23 The results of Guagliano [40] and inverse analysis of the residual z-direction stress distribution in the Almen strip using Eq. (1). **a** inverse analysis using FEM results, and **b** inverse analysis using experimental results

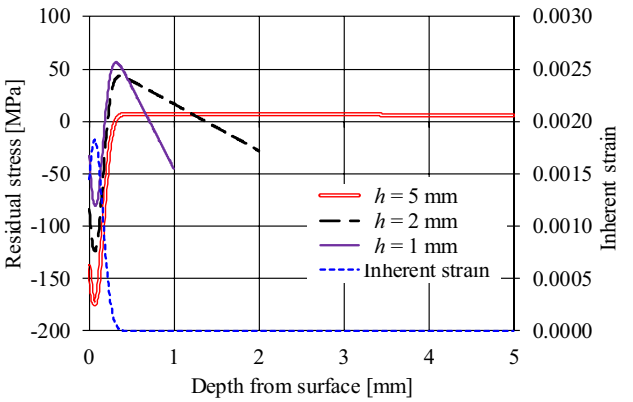

Fig. 24 Effect of thickness on residual stress distribution analyzed by inherent strain distribution approximated at $h=5$ mm using Eqs. (8)–(10) when $D=0.3$ mm and $V=30$ m/s

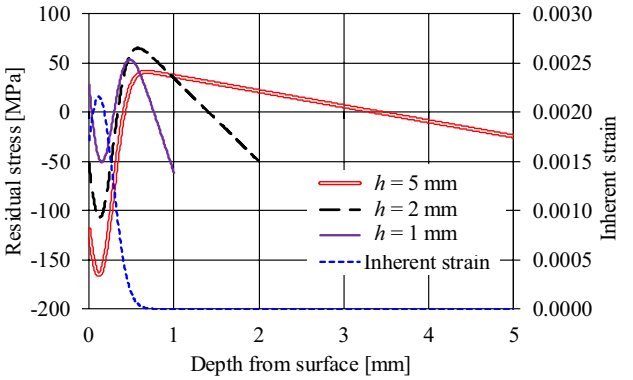

Fig. 25 Effect of thickness on residual stress distribution analyzed by inherent strain distribution approximated at $h=5$ mm using Eqs. (8)–(10) when $D=0.3$ mm and $V=65$ m/s

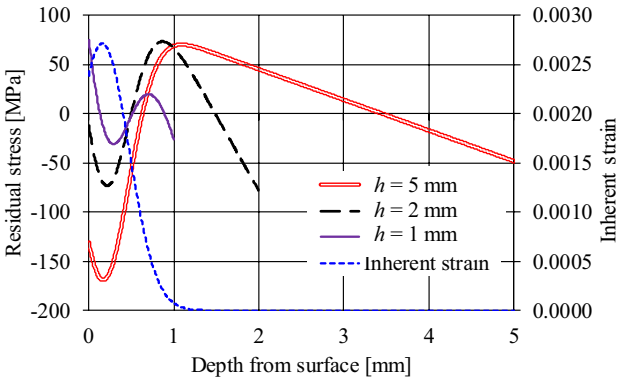

Fig. 26 Effect of thickness on residual stress distribution analyzed by inherent strain distribution approximated at $h=5$ mm using Eqs. (8)–(10) when $D=0.7$ mm and $V=35$ m/s

obtained at $h=5$ mm when $D=0.3$ mm, and $V=30$ m/s shown in Figs. 7, 13, and 14. Figure 25 demonstrates the effect of thickness on the residual stress distribution analyzed using inherent strain obtained at $h=5$ mm when $D=0.3$ mm, and $V=65$ m/s shown in Figs. 7, 15, and 16. Figure 26 demonstrates the effect of thickness on the residual stress distribution analyzed using inherent strain obtained at $h=5$ mm when $D=0.7$ mm, and $V=35$ m/s shown in Figs. 17, 18, and 19.

Even under the same peening conditions, the residual stress distribution is different when the thickness h is different. As the h becomes thinner, the bending deformation increases; therefore, the compressive residual stress on the peened surface decreases and the compressive stress is generated on the back surface. This tendency becomes more pronounced as the depth of the inherent strain increases. In the case of $h=1$ mm shown in Fig. 26, the depth of the inherent strain is 1 mm or more, and the residual stress at the peened surface is tensile. On the other hand, in Fig. 20 and 21, the thickness is 50 mm; therefore, no effect of bending deformation exists.

The residual stress distribution varies depending on the thickness and peening condition; however, the inherent

strain distribution is determined by the peening condition. As shown in Fig. 26, this method is valid even when the inherent strain depth is greater than the thickness. The advantage of this method is that the residual stress distribution under different shot peening conditions and thicknesses can be predicted by setting approximate equations of the inherent strain distribution in a small number of numerical simulations or experiments. For example, this method can be used for shot peening of unevenly textured parts, such as aircraft parts. By inputting the inherent strain distribution to the FE model using the composite shell, as shown in Fig. 3, the residual stress distribution of a complex structure can be calculated.

9 Conclusion

The residual stress distributions in aluminum–magnesium alloy plates at various shot velocities and shot diameters were analyzed using a nonlinear elastic–plastic finite element method and experimentally verified via measurements. Based on these results, a quantitative equation for the inherent strain distribution for a wide range of shot velocities and shot diameters was developed for the analytical prediction of the residual stress distribution. The following conclusions can be drawn.

(1) The inherent strain distribution is inversely identified from the residual stress distribution simulated using the nonlinear elastic–plastic finite element method.
(2) The inherent strain distribution is presented as a Gaussian distribution, and its three coefficients can be approximated using a quadratic equation of the shot velocity and a power-law equation of the shot diameter.
(3) The residual stress distribution analyzed using the inherent strain under the new shot peening conditions is consistent with the experimental results. This analysis method can be applied to experimental results obtained using different shot blasting machines.
(4) Because the inherent strain distribution is not affected by thickness, the inherent strain obtained in the 5 -mm-thick plate is the same as that in a plate of different thickness. The different residual stress distributions at thicknesses of 5, 2 and 1 mm can be analyzed using the same inherent strain distribution. The advantage of this method is that the estimated inherent strain distribution can be used to predict the residual stress distribution for thicknesses that have not been tested or simulated.
(5) The proposed method can also be applied to residual stress distributions in alloy steels. The method is applicable both aluminum alloy and steel.

Acknowledgements This study was supported by JSPS KAKENHI Grant No. 20K05158, and the Amada Foundation Grant No. AF-2020019-B3. The authors would like to thank Mr. Naoki Kono, Mr. Takanori Murakami, and Mr. Jaxin He, graduate students at Tokai University, for their assistance with the experiments.

Author contribution Takahiro Ohta: Investigation, Writing—original draft. Ninshu Ma: Review & editing, Validation.

Funding This study was supported by JSPS KAKENHI Grant No. 20K05158, and the Amada Foundation Grant No. AF-2020019-B3.

Declarations

Competing interest The authors declare no conflicting interests.

References

1. Schiffner K, Helling C (1999) Simulation of residual stresses by shot peening. Comput Struct 72(1–3):329–340. https://doi.org/10.1016/S0045-7949(99)00012-7
2. Tao X, Gao Y (2021) Influences of thermal effects on residual stress fields of an aluminum-lithium alloy induced by shot peening. Int J Adv Manuf Technol 112(11–12):3105–3116. https://doi.org/10.1007/s00170-020-06557-3
3. Gallitelli D, Boyer V, Gelineau M, Colaitis Y, Rouhaud E, Retraint D, Kubler R, Desvignes M, Barrallier L (2016) Simulation of shot peening: From process parameters to residual stress fields in a structure. Comptes Rendus Mécanique 344(4–5):355–374. https://doi.org/10.1016/j.crme.2016.02.006
4. Li K, Wang C, Hu X, Zhou Y, Lai Y, Wang C (2022) DEM-FEM coupling simulation of residual stresses and surface roughness induced by shot peening of TC4 titanium alloy. Int J Adv Manuf Technol 118(5–6):1469–1483. https://doi.org/10.1007/s00170-021-07905-7
5. Wang S, Li Y, Yao M, Wang R (1998) Compressive residual stress introduced by shot peening. J Mater Process Technol 73(1–3):64–73. https://doi.org/10.1016/S0924-0136(97)00213-6
6. Zinn W, Scholtes B (2005) Influence of shot velocity and shot size on Almen intensity and residual stress depth distributions. Proc 9th Int Conf Shot Peening:379–384. https://www.shotpeener.com/library/pdf/2005113.pdf. Accessed 20 Aug 2023
7. Miao HY, Demers D, Larose S, Perron C, Lévesque M (2010) Experimental study of shot peening and stress peen forming. J Mater Process Technol 210(15):2089–2102. https://doi.org/10.1016/j.jmatprotec.2010.07.016
8. Al-Hassani STS (1981) Mechanical aspects of residual stress development in shot peening. Proc 2nd Int Conf Shot Peening: 583–602. https://www.shotpeener.com/library/pdf/1981050.pdf. Accessed 20 Aug 2023
9. Al-Obaid YF (1990) A rudimentary analysis of improving fatigue life of metals by shot-peening. J Appl Mech Trans ASME 57(2):307–312. https://doi.org/10.1115/1.2891990
10. Ogawa K, Asano T (2000) Theoretical prediction of residual stress produced by shot peening and experimental verification for carburized steel. J Soc Mater Sci Jpn 49(3):55–62 (in Japanese). https://doi.org/10.2472/jsms.49.3Appendix_55.
11. Robertson GT (1997) The effect of shot size on the residual stresses, resulting from shot peening. Shot Peener Mag 11(3):46–47. https://www.shotpeener.com/library/pdf/1997050.pdf. Accessed 20 Aug 2023

12. Ohta T, He J, Takahashi S, Ma N (2023) Measurement and identified prediction equation for residual stress distribution in aluminum Alloy A5052 under various pneumatic shot peening conditions. J Mater Eng Perform:1–13. https://doi.org/10.1007/s11665-023-08031-z
13. Fujimoto T (1970) A method for analysis of residual welding stresses and deformations based on the inherent strain - A theoretical study of residual welding stresses and deformations (Report 1). J Jpn Welding Soc 39(4):236–252 (in Japanese). https://doi.org/10.2207/qjjws1943.39.4_236.
14. Ueda Y, Ma N (1994) Estimating and Measuring Methods of Residual Stresses Using Inherent Strain Distribution Described as Functions (Report 1), Expression of Inherent strain in Form of Function and Its Estimation. Trans Welding Research Institute of Osaka University 23(1):71–78
15. Nakacho K, Ogawa N, Ohta T, Nayama M (2014) Inherent-strain-based theory of measurement of three-dimensional residual stress distribution and its application to a welded joint in a reactor vessel. ASME J Pressure Vessel Technol 136(3):031401. https://doi.org/10.1115/1.4026496
16. Korsunsky AM, Regino GM, Nowell D (2007) Variational eigenstrain analysis of residual stresses in a welded plate. Int J Solids Struct 44(13):4574–4591. https://doi.org/10.1016/j.ijsolstr.2006.11.037
17. Niku-Lari A (1981) Methode de la fleche methods de la source des contraintes residuelles. Proc 1st Int Conf Shot Peening 237–247. https://www.shotpeener.com/library/pdf/1981051.pdf. Accessed 20 Aug 2023
18. Terasaki T, Chen J, Akiyama T, Kishitake K (1999) Non-destructive method for estimating residual stress distribution in component due to shot peening. JSME Int J Ser A Solid Mech Mater Eng 42(2):216–223. https://doi.org/10.1299/jsmea.42.216
19. Kitamura K, Terasaki T, Akiyama T (2000) Effect of grain shapes on residual stress distribution due to shot peening. J Soc Mat Sci Jpn 49(6):651–654. https://doi.org/10.2472/jsms.49.651
20. Korsunsky AM (2005) The modelling of residual stresses due to surface peening using eigenstrain distributions. J Strain Anal Eng Des 40(8):817–824. https://doi.org/10.1243/030932405X30984
21. Korsunsky AM (2008) Residual elastic strain due to laser shock peening: modelling by eigenstrain distribution. J Strain Anal Eng Des 41(3):195–204. https://doi.org/10.1243/03093247JSA141
22. Achintha M, Nowell D (2011) Eigenstrain modellingof residual stresses generated by arrays of LSP shots. Procedia Eng 10:1327–1332. https://doi.org/10.1016/j.proeng.2011.04.221
23. Coratella S, Sticchi M, Toparli MB, Fitzpatrick ME, N. Kashaev N (2015) Application of the eigenstrain approach to predict the residual stress distribution in laser shock peened AA7050-T7451 samples. Surf Coat Technol 273:39–49. https://doi.org/10.1016/j.surfcoat.2015.03.026
24. Song X, Liu WC, Belnoue JP, Dong J, Wu GH, Ding WJ, Kimber SAJ, Buslaps T, Lunt AJG, Korsunsky AM (2012) An eigenstrain-based finite element model and the evolution of shot peening residual stresses during fatigue of GW103 magnesium alloy. Int J Fatigue 42:284–295. https://doi.org/10.1016/j.ijfatigue.2012.01.019
25. Salvati E, Korsunsky AM (2018) A simplified FEM eigenstrain residual stress reconstruction for surface treatments in arbitrary 3D geometries. Int J Mech Sci 138–139:457–466. https://doi.org/10.1016/j.ijmecsci.2018.02.016
26. Faucheux PA, Gosselin FP, Lévesque M (2018) Simulating shot peen forming with eigenstrains. J Mater Process Technol 254:135–144. https://doi.org/10.1016/j.jmatprotec.2017.11.036
27. Hu Y, Li Z, Yu X, Yao Z (2015) Effect of elastic prestress on the laser peen forming of aluminum alloy 2024–T351: Experiments and eigenstrain-based modeling. J Mater Process Technol 221:214–224. https://doi.org/10.1016/j.jmatprotec.2015.02.030
28. Ohta T, Sato Y (2021) Numerical analysis of peen forming for high-strength aluminum alloy plates. Mater Trans 62(6):846–855. https://doi.org/10.2320/matertrans.P-M2021818
29. Ohta T, Sato Y (2022) Effect of saturation peening on shape and residual stress distribution after peen forming. Int J Adv Manuf Technol 119(7–8):4659–4675. https://doi.org/10.1007/s00170-021-08473-6
30. Ohta T (2020) Peen forming of anisotropic double-curved surface by vibration peening using rectangular solid pin. Mater Trans 61(1):162–168. https://doi.org/10.2320/matertrans.P-M2019853
31. Miao HY, Lévesque M, Gosselin FP (2023) Eigenstrain-based analysis of why uniformly shot peened aluminium plates bend more in the rolling direction. Strain:e12451. https://doi.org/10.1111/str.12451
32. Ohta T, Ma N (2020) Shot velocity measurement using particle image velocimetry and a numerical analysis of the residual stress in fine particle shot peening. J Manuf Process 58:1138–1149. https://doi.org/10.1016/j.jmapro.2020.08.059
33. Ohta T, Tsutsumi S, Ma N (2021) Direct measurement of shot velocity and numerical analysis of residual stress from pneumatic shot peening. Surf Interfaces 22:100827. https://doi.org/10.1016/j.surfin.2020.100827
34. Zupanc U, Grum J (2010) Effect of pitting corrosion on fatigue performance of shot-peened aluminium alloy 7075–T651. J Mater Process Technol 210(9):1197–1202. https://doi.org/10.1016/j.jmatprotec.2010.03.004
35. Aghaie-Khafri M, Amin M, Momeni AH (2012) Life Assessment and Life Extension of an Aircraft Wheel. Adv in Mech Eng 4:326971. https://doi.org/10.1155/2012/326971
36. Tanaka K (2019) The cos α method for X-ray residual stress measurement using two-dimensional detector. Mech Eng Rev 6(1):18–00378. https://doi.org/10.1299/mer.18-00378
37. Moore MG, Evans WP (1958) Mathematical correction for stress in removed layers in X-ray diffraction residual stress analysis. SAE Trans 66:6340–6345. https://doi.org/10.4271/580035
38. Yasukawa S, Ohya S, Tango K, Takeda K, Tange A (2014) Microscopic residual stress distribution measurement on the surface of shot peening. J Soc Mater Sci Jpn 63(9):655–661. https://doi.org/10.2472/jsms.63.655
39. Géron A (Shimoda N, Nagao T Transl) (2020) Hands-on machine learning with Scikit-Learn, Keras, and TensorFlow, 2nd edition. 155–175, O'Reillly Japan
40. Guagliano M (2001) Relating Almen intensity to residual stresses induced by shot peening: a numerical approach. J Mater Process Technol 110(3):277–286. https://doi.org/10.1016/S0924-0136(00)00893-1
41. Ohta T, Inoue A (2019) Measurement and functional approximation of peening intensity distributions. Mater Trans 60(6):1004–1010. https://doi.org/10.2320/matertrans.P-M2019816